Int. J. Electrochem. Sci., 14 **(2019)** 3568 – 3580, doi: 10.20964/2019.04.53

International Journal of
ELECTROCHEMICAL
SCIENCE
www.electrochemsci.org

Facile Solvothermal Preparation and Electrochemical Properties of Fe-doped $CaTi_2O_4(OH)_2$ for Supercapacitors

Qifu Bao, Weixia Dong[*]*, Xingyong Gu, Jijun Shi and Huijuan Shen*

Department of Material Science and Engineering, Jingdezhen Ceramic Institute, Jingdezhen, 333001, P. R. China
[*]E-mail: weixia_dong@sina.com

Received: 20 December 2018 / *Accepted:* 28 January 2019 / *Published:* 10 March 2019

Fe-doped $CaTi_2O_4(OH)_2$ cathode materials for supercapacitors were synthesized by a facile hydrothermal method. The effects of Fe-doping ion content on the electrochemical performance of $CaTi_2O_4(OH)_2$ were studied by galvanostatic charge/discharge and cyclic voltammetry measurements. The optimal Fe-doping ion content x was 0.06 in a $CaFe_xTi_{2-x}(OH)_2$ system. Fe-doped $CaTi_2O_4(OH)_2$ samples exhibited improved cyclic ability, such that the capacity of $CaFe_{0.06}Ti_{1.94}O_4(OH)_2$ was 964.3 $F{\cdot}g^{-1}$, which was 3.36-fold higher than the undoped system, at a current density of 10 $A{\cdot}cm^{-2}$, and had good long-term cycling stability (99.7% retention after 5000 cycles at 10 $mA{\cdot}cm^{-2}$). The enhanced electrochemical properties of $CaTi_2O_4(OH)_2$ might be ascribed to material morphology, increased electrical conductivity, and structural stability.

Keywords: Fe-doped contents, $CaTi_2O_4(OH)_2$, electrochemical properties, supercapacitors

1. INTRODUCTION

As a means of bridging the power-energy gap between batteries and traditional capacitors, rechargeable supercapacitors (SC) have attracted interest as an energy storage system due to their high rate capacity and high power density. [1–4] The electrode material is a key component in SCs, because charge generation and transport take place through it. [5–6] Metal oxides and hydroxides have been studied extensively [7–17], however, these materials cannot meet the rapid development of the current information-rich mobile society, due to their relatively low rate capability, cycling stability, or high expense. For example, in a commercial SC, Ru oxide is utilized as the cathode material, but its high cost prevents large-scale use. Therefore, more effort has been invested in exploring novel electrode materials for both cathodes and anodes. [18–21] $CaTi_2O_4(OH)_2$ has a lamellar structure with periodic

stacking of positively charged (M^{II}, M^{III})$(OH)_2$ octahedral layers related to brucite. The sheets are bonded together via interlayer anions and water molecules. Low cost, easy preparation, and low toxic properties of $CaTi_2O_4(OH)_2$ are its main advantages. Recently, $CaTi_2O_4(OH)_2$ nanosheets have been shown to exhibit good electrical properties and facile to produce in large scale. [22–24]. Despite its economic advantages, according to our previous report, it is necessary to improve the material's low conductivity to enhance energy conversion efficiency. Generating active sites and enhancing intrinsic conductivity in defect engineering of transition metal dichalcogenides have been regarded an effective method for improving electrochemical performance. To our knowledge, the partial substitution of Ti with other metals (e.g., Fe ions) was also worth exploring, as doping of Fe ions into $LiMn_2O_4$, $Li_3V_2(PO_4)_3$, and $Li_2Ti_3O_7$ have been shown to effectively enhance their electronic conductivity, due to formed vacancies. [25–27] In this paper, the effects of Fe ion doping on the electrochemical properties of $CaTi_2O_4(OH)_2$ were examined.

2. EXPERIMENTAL

2.1. Synthesis of the samples

Titanium *n*-butoxide (TBOT), ferric nitrate ($Fe(NO_3)_3 \cdot 9H_2O$), and calcium chloride ($CaCl_2$) were chosen to form the precursor. The molar ratio of precursor $CaCl_2$/TBOT/water/ethanol was 1/1/100/10. For this, a TBOT-ethanol solution was added to an aqueous $CaCl_2$ and $Fe(NO_3)_3 \cdot 9H_2O$ solution (Fe/Ti molar ratio x was 0, 0.02, 0.04, 0.06, and 0.08), forming suspension A. After stirring for 10 min, 2.4 ml of 3 M NaOH was added to suspension A under vigorous stirring. Subsequently, the autoclave was sealed and heated to 200°C for 24 h, followed by natural cooling to room temperature. The samples were thoroughly washed and dried at a vacuum oven at 80°C for 24 h. The powders with various Fe ion doping concentrations were prepared, hereafter termed as $CaFe_xTi_{2-x}(OH)_2$ (x = 0, 0.02, 0.04, 0.06, and 0.08).

2.2. Characterization of the samples

Phases of samples were analyzed by X-ray diffraction (XRD; X'Pert Pro, Malvern Panalytical B.V., Almelo, The Netherlands) in a θ range from 10 to 70°, using Cu-K_a radiation (λ = 0.15420 nm). Sample microstructures were analyzed by a field emission scanning electron microscopy (FESEM; Hitachi S-4800, Hitachi High-Technologies Corp., Tokyo, Japan) and high-resolution transmission electron microscopy (HRTEM, FEI Tecnai G2 F-30, FEI Co., Hillsboro, OR, USA) operating at an accelerating voltage of 200 kV to further characterize sample morphology. Sample surface areas were characterized using the Brunauer-Emmett-Teller (BET) method and pore sizes determined using the Barrett-Joyner-Halenda (BJH) method with the nitrogen branches of isotherms collected at 77 K on a TriStar II 3020 nitrogen adsorption apparatus (Micromeritrics Instrument Corp., Norcross, GA, USA).

2.3. Electrochemical measurement of the samples

Working electrodes were prepared by coating a mixture of 85-wt% $CaFe_xTi_{2-x}(OH)_2$ sample, 10-wt% acetylene black, and 5-wt% poly(tetrafluoroethylene) onto nickel foam sheets. The electrolyte was 1 M $LiPF_6$ (battery grade; Merck KGaA, Darmstadt, Germany) in a mixture of ethyl carbonate (EC) and diethyl carbonate (DMC, 1/1 by vol) on nickel foam sheets with a size of 1.5 × 1.5 cm and dried at 60°C (8.4 mg loading). Electrochemical properties were measured using CHI660C electrochemical analyzer system (Chenhua Instrument Corp., Shanghai, China) in a three-compartment cell with a working electrode, platinum plate counter electrode, and saturated calomel reference electrode (SCE). Galvanostatic charge-discharge was analyzed using a LAND CT2001A test system (Land electronics Co., Ltd., Wu Han, China).

3. RESULTS AND DISCUSSION

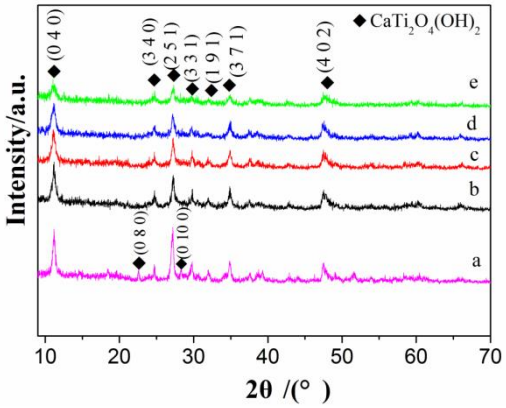

Figure 1. XRD patterns of $CaTi_2O_4(OH)_2$ samples prepared with different Fe-doped ions contents: (a) 0, (b) 0.02, (c) 0.04, (d) 0.06 and (e) 0.08.

XRD patterns of typical $CaFe_xTi_{2-x}(OH)_2$ samples (x = 0, 0.02, 0.04, 0.06, and 0.08) showed that the peaks corresponded to $CaTi_2O_4(OH)_2$ (JCPDS card 39-0357, Fig. 1). No other impurity peaks were observed, indicating that pure $CaTi_2O_4(OH)_2$ had been obtained. Peak positions of doped samples were consistent with undoped samples, although sample peak intensities varied. The intensities of (040), (340), (331), (191), (371), and (402) for doped samples were much lower than those of undoped samples, which might be attributed to solid-solid interactions and altered grain size. [28] The sample lattice constants with various Fe-doped contents showed that the intensities of Fe-doped samples decreased with Fe-doped content and Fe ion peaks were not observed (Fig. 1). The average crystallite size of $CaTi_{2-x}Fe_xO_4(OH)_2$ samples with various x values was calculated using the XRD-Scherrer formula, $d = k\lambda/\beta\cos\theta$, where d is the mean crystallite size, k at -0.9, λ the wavelength of Cu-K_α (e.g., λ = 0.15420 nm), β the full width at half maximum intensity of the peak (FWHM) in radians, and θ Bragg's diffraction angle [28]. The lattice constants and cell volumes were calculated by direct methods and Fourier synthesis using the program SHELXS−97 (Program for Crystal Structure Solution and Refinement, University of Gottingen, Germany) [29]. The crystalline size and cell

volume were observed to decrease with increased *x* (Table 1), which indicated that Fe ions had inserted into the interlayer of $CaTi_2O_4(OH)_2$, due to the smaller ion radius of Fe^{3+} (0.69 A), compared to Ti^{4+}(0.745 A). When various Fe-doped ions contents were introduced, all diffraction peaks were seen to broaden to different degrees. These results indicated that Fe-doped ions might have lowered the crystal size of $CaTi_2O_4(OH)_2$, which was further confirmed by the following SEM and TEM results.

Table 1. Cell parameters and specific surface areas of $CaFe_xTi_{2-x}(OH)_2$ samples with various x

x (mol)	Crystalline size (nm)	Lattice constant/ Å			Cell volume Å^3	Specific surface areas (m^2/g)
		a	b	c		
0	50.1	12.09277	31.65766	4.93451	1894.49	112.8
0.02	45.5	12.09280	31.66751	4.94257	1894.92	121.7
0.04	19.0	12.09283	31.69754	4.94856	1897.08	148.7
0.06	15.4	12.09287	31.69790	4.95939	1897.20	153.1

Typical sample FESEM images showed that, compared with undoped samples, doped samples exhibited smaller sizes and some small particles observed (Table 1, Fig. 2). Typical images of an undoped sample showed many small, distributed nanosheets (Fig. 2a). When the Fe-doped content was 0.06 mol, the sample exhibited uniformly dispersed, small nanosheets. When *x* was 0.08, large agglomerates composed of dense nanosheet-like morphology appeared in the samples while well-dispersed nanosheets disappeared (Figs. 2e–2f), indicating that excessive Fe-doped content was harmful for the formation of high-quality nanosheet structures. This was attributed to the effect that Fe-doping ions made the nucleation process more difficult as clarified that the degree of crystallization decreases (Fig. 1).

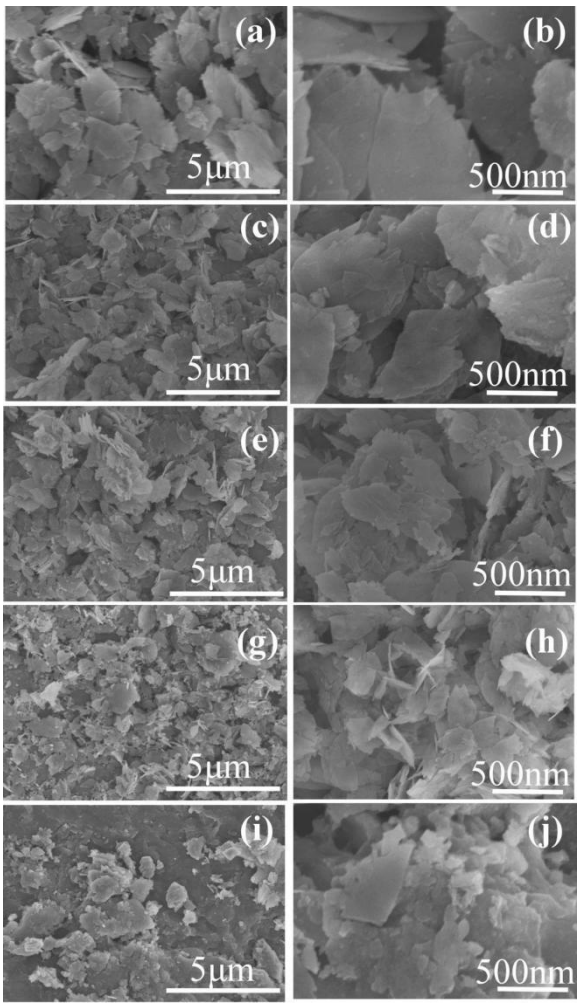

Figure 2. FESEM images of the $CaTi_2O_4(OH)_2$ sample prepared with different Fe-doped ions contents: (a) 0, (b) 0.02, (c) 0.04, (d) 0.06, (e) 0.08.

Typical TEM images and corresponding HRTEM patterns of $CaFe_xTi_{2-x}O_4(OH)_2$ samples with x = 0 and 0.06 showed that undoped $CaTi_2O_4(OH)_2$ samples were composed of many overlapped nanosheets of 5–7 nm thickness (Fig. 3a). HRTEM images of undoped $CaTi_2O_4(OH)_2$ samples showed that the lattice space was 0.1898 nm, which was in accordance with a lattice spacing of the (422) plane (Fig. 3b). TEM images of $CaFe_{0.06}Ti_{1.94}O_4(OH)_2$ samples showed that most of the sample retained nanosheet-like structures with thicknesses of 3–5 nm and some nanoparticles coexisted, in which some mesopores formed (Fig. 3c). Although $CaFe_{0.06}Ti_{1.94}O_4(OH)_2$ samples retained the original flake structure, its thickness was smaller than that of undoped sample and filled with small pores, which was beneficial to ion adsorption from the electrolyte. Thus, the BET of the samples was observed to increase with x (Table 1) and, thus, the samples' electrochemical properties enhanced. After doping with Fe ions, $CaFe_{0.06}Ti_{1.94}O_4(OH)_2$ nanosheets also exhibited clear lattice fringes and the corresponding lattice spacing 0.1890 nm, which was accordance with a (422) plane (Fig. 3d).

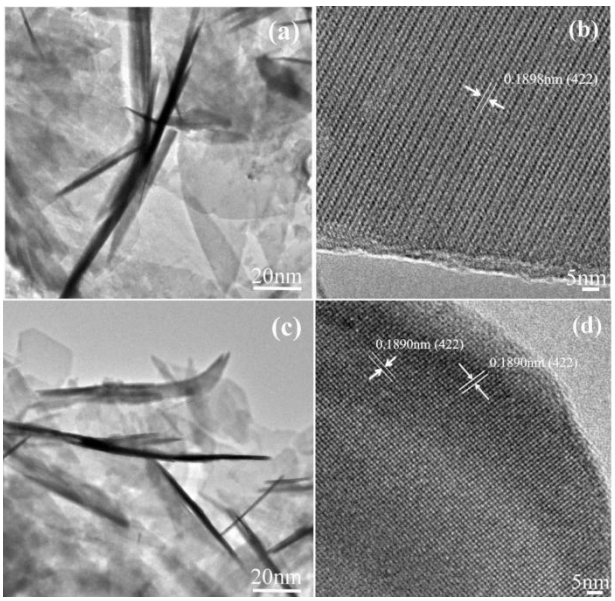

Figure 3. TEM images and the corresponding HRTEM patterns of $CaFe_{0.06}Ti_{1.94}O_4(OH)_2$ samples with x=0 and 0.06, respectively.

The specific surface areas of $CaFe_xTi_{2-x}O_4(OH)_2$ (x = 0, 0.02, 0.04, 0.06, and 0.08) samples were 108.9, 113.6, 123.7, 148.7, and 56.3 m^2/g, respectively (Table 1). Clearly, suitable Fe-doping enhanced the specific surface areas of $CaTi_2O_4(OH)_2$ samples to various degrees. Isotherms of typical samples showed that both samples exhibited distinct hysteresis loops, which was accordance with a type IV pattern, indicating their mesoporous structure that might have contributed to interspaces among $CaTi_2O_4(OH)_2$ nanosheets (Fig. 4). The pore size distribution of the typical samples revealed that, Fe-doped samples exhibited smaller size distributions, with mean pore diameters of ~6.8 nm, which was attributed to spaces between small $CaTi_2O_4(OH)_2$ grains (Fig. 4, inset). Such a small mesoporous size distribution was conductive for electrolyte adsorption and diffusive ion transportation.

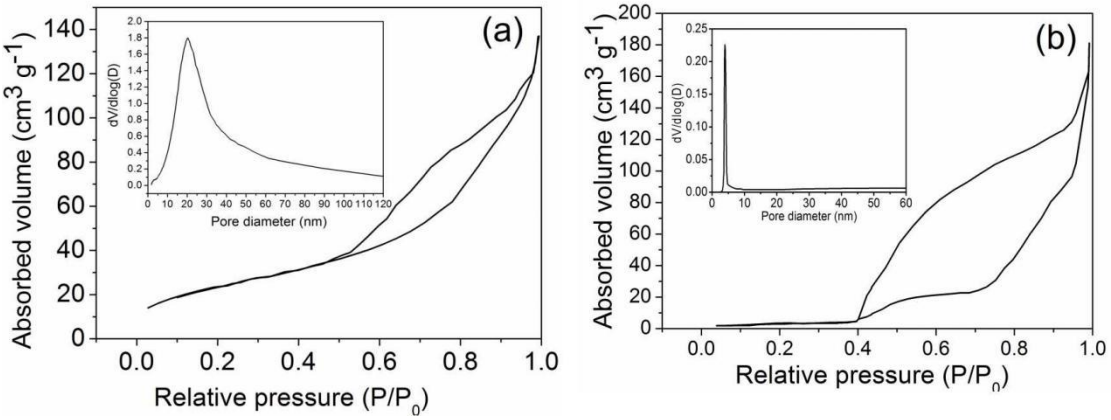

Figure 4. The isotherms and pore size distribution of the typical $CaFe_xTi_{2-x}O_4(OH)_2$ samples with x=0 and 0.06, respectively.

The oxidation states of Fe and Ti in $CaFe_{0.06}Ti_{1.94}O_4(OH)_2$ samples were studied using XPS. XPS. Fe-2*p* and Ti-2*p* peaks for $CaFe_{0.06}Ti_{1.94}O_4(OH)_2$ clearly showed that two main peaks at ~459.0 and 464.8 eV in the spectra, which were ascribed to Ti-$2p^{3/2}$ and Ti-$2p^{1/2}$, respectively, corresponding to the Ti^{4+} oxidation state (Fig. 5). This might be attributed to spin-orbit splitting of Ti-2*p*. At the same time, the peak at ~710 eV matched well with an observed peak in Fe_2O_3, [30] where the two peaks at 711.1 and 724.7 eV were attributed to Fe-$2p^{3/2}$ and Fe-$2p^{1/2}$ (Fig. 5a), respectively. [27] In addition, the energy difference between Fe-$2p^{3/2}$ and Fe-$2p^{1/2}$ was 13.6 eV, which is typical for the Fe^{3+} state. Therefore, it was concluded that Fe ions doped into $CaTi_2O_4(OH)_2$ existed in trivalent form, which indicated that some Fe^{3+} diffused into titania lattices and substituted for Ti^{4+} in the lattice. After Fe^{3+} ($0 < x \leq 0.06$) partially replaced Ti^{4+}, Fe doped $CaTi_2O_4(OH)_2$ samples had a smaller lattice parameter. Fe^{3+} ions located in pseudotetrahedral sites in TiO_2-layers or in square-pyramidal sites (in CaO-layers) formed with the participation of oxygen vacancies [31]. Fe ion stabilization on $CaTi_2O_4(OH)_2$ lattices might have been due to the smaller Fe^{3+} ion radius than that of Ti^{4+} (0.69 and 0.745 Å, respectively), which enhanced the attractive action between central cations and oxygen anions and, thus, enhanced the stability of nanosheet-like structures to ion absorption/desorption. Fe-doped $CaTi_2O_4(OH)_2$ samples with *x* at 0.02, 0.04, and 0.06 mol exhibited much better electrochemical properties than undoped $CaTi_2O_4(OH)_2$, which was attributed to the solid solution formation of Fe^{3+} ion replacement of Ti^{4+}, which resulted in lattice distortion and a certain amount of oxygen vacancy in the sample, due to the imbalance of electricity values. After further doping Fe ions to 0.08 mol, there was a continuous redistribution of Fe^{3+} ions, which thus caused axial stresses in the layers. Fe cluster formation was harmful for the electrochemical properties of $CaTi_2O_4(OH)_2$. Based on CV results, the electrode reaction reversibility was improved with the appropriate Fe-doping of $CaTi_2O_4(OH)_2$.

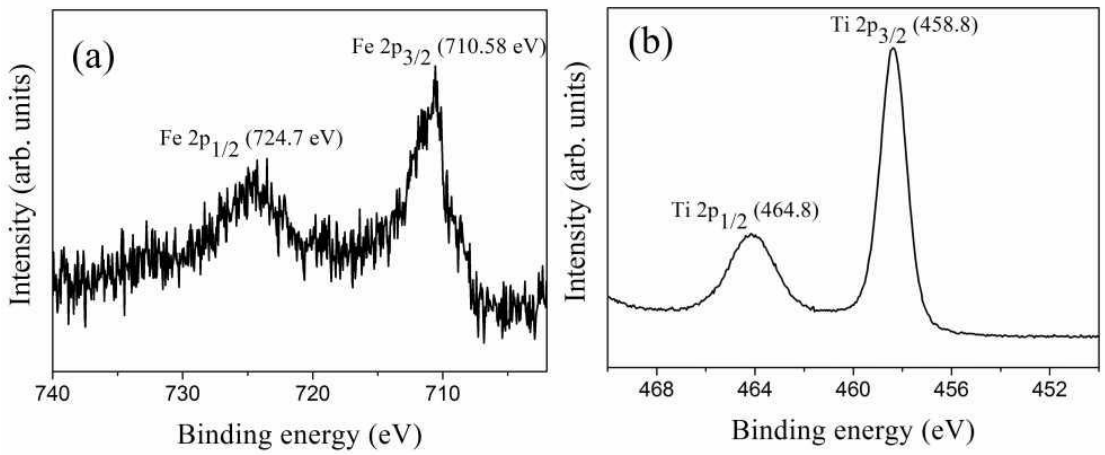

Figure 5. High-resolution XPS survey of $CaFe_{0.06}Ti_{1.94}O_4(OH)_2$: (a) Fe 2*p*, (b) Ti 2*p*.

CV curves of electrodes prepared from $CaFe_xTi_{2-x}O_4(OH)_2$ samples (x = 0, 0.02, 0.04, 0.06, and 0.08) showed that areas surrounded by CV curves and peak currents of doped samples were much larger than those of undoped samples, indicating that all Fe-doped $CaTi_2O_4(OH)_2$ samples exhibited larger discharge capacities than those of undoped samples (Fig. 6a). Interestingly, CV curve shapes after Fe-doped $CaTi_2O_4(OH)_2$ samples were almost unchanged, which indicated that Fe-doped

$CaTi_2O_4(OH)_2$ did not change the material's structure and also indicated the electrochemical reaction process for the phase transformation and redox couple. However, the cathodic peaks all shifted to lower potentials and then the potential differences between anodic and cathodic peaks became smaller, indicating an improvement in electrode reaction reversibility. Moreover, the symmetry of redox peaks from Fe-doped samples was observed to be relatively higher than that of undoped ones, which indicated that sample capacity stability was enhanced after Fe doping. Charge-discharge curves of $CaTi_2O_4(OH)_2$ electrodes in the range of 0–0.5 V at 10 $mA \cdot cm^{-2}$ are shown in Figure 6b. Based on the data in Figure 6(a), the specific capacitance was calculated according to equation (1)

$$C = (I \Delta t)/(m \Delta v) \qquad (1)$$

where I is the charge or discharge current (A), m the mass of active material in the electrode (mg), Δv the voltage difference between the upper and lower potential limits (V), Δt the charge or discharge time (s), and C the specific capacitance ($F \cdot g^{-1}$). The specific capacitance of $CaTi_2O_4(OH)_2$ electrodes prepared from $CaTi_2O_4(OH)_2$ samples (x = 0, 0.02, 0.04, 0.06, 0.08), calculated from the discharge curves, were 287.3, 498.9, 810.9, 964.3, and 351.2 $F \cdot g^{-1}$ at the discharge current of 10 $mA \cdot cm^{-2}$, respectively. $CaTi_{1.94}Fe_{0.06}O_4(OH)_2$ electrodes possessed a larger specific capacitance than those of Fe-doped $CaTi_2O_4(OH)_2$ electrodes at each current density, which was consistent with their CV results .

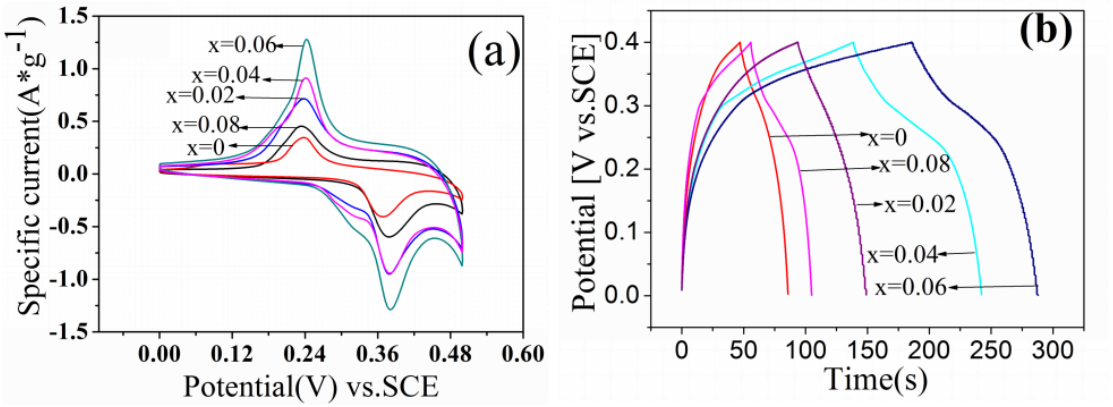

Figure 6. (a) The cyclic voltammogram (CV) curves and (b) the charge-discharge curves of the electrode samples prepared from $CaTi_{2-x}Fe_xO_4(OH)_2$ samples (x=0, 0.02, 0.04, 0.06, 0.08)

Nyquist plots of the optimal $CaFe_{0.06}Ti_{1.94}O_4(OH)_2$ electrode and an original sample, in the range of 1–1000 kHz, showed that these impedance spectra exhibited high frequency semicricles and low frequency tails, suggesting a double layer reaction at electrode/sample interfaces and ion diffusion in the solid matrices (Fig. 7). In the high frequency region, both samples were seen to exhibit similar semicircles, corresponding to the charge-transfer resistance.[31] Compared to the undoped sample, the charge-transfer resistance (Rct) of Fe-doped samples decreased. Combined with XRD, HRTEM, and the decreased cell volumes of Fe-doped samples results (Table 1), the small grain sizes and pores of Fe-doped samples were concluded to provide more channels and interface between electrode and electrolyte for fast ion and charge transport. The straight line in the low frequency region was ascribed to Warburg impedance. [32] Resistance values of undoped samples were ~75 $\Omega \cdot cm^2$, whereas the

semicircle was smaller and resistance values thus lower after doping with Fe ions. This indicated that Fe doped samples had faster charge transfer at the electrode-electrolyte interface, compared to without doping. An equivalent electrical circuit model for illustrating impedance spectra was proposed here, which was composed of electrolyte resistance (*R*s), charge-transfer resistance (Rct), double layer capacitance, a constant phase element (CPE), with Warburg impedance (Zw) attributed to ion diffusion in the matrix (Fig. 7d, inset). In this, the *R*ct of all Fe-doped samples was smaller than that of undoped $CaTi_2O_4(OH)_2$ electrodes, which might have been ascribed to Fe doping in the $CaTi_2O_4(OH)_2$ electrode. The *R*ct of the $CaFe_{0.06}Ti_{1.94}O_4(OH)_2$ cathode was the smallest at 2.41 $\Omega \cdot cm^2$. This indicated that the resistance of Fe-doped $CaTi_2O_4(OH)_2$ electrodes was reduced by increased conductivity. $CaFe_{0.06}Ti_{1.94}O_4(OH)_2$ samples exhibited a combination of Ti^{4+}/Ti^{3+} redox couples at relatively low potential, which significantly induced irreversibility of these electrodes. [23–24]

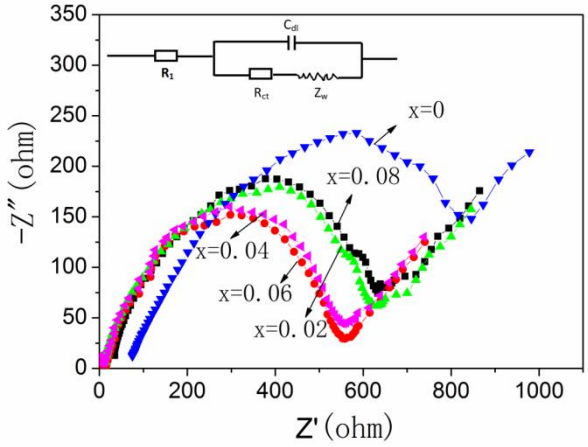

Figure 7. The typical Nyquist plots of the electrodes made from the as-prepared $CaTi_{2-x}Fe_xO_4(OH)_2$ samples (x=0, 0.02, 0.04, 0.06, 0.08). Inset of Fig. 7 is equivalent circuit model.

Representative CV curves of $CaFe_{0.06}Ti_{1.94}O_4(OH)_2$ electrodes at various scan rates and from 10 to 70 $mV \cdot s^{-1}$ showed that redox peak currents increased with the scan rate, suggesting rapid reversible redox reactions on $CaFe_{0.06}Ti_{1.94}O_4(OH)_2$ during the charge/discharge process (Fig. 8a). Moreover, anodic peak potentials increased and cathodic potentials decreased with high scan rates. The galvanostatic charge-discharge curves of $CaFe_{0.06}Ti_{1.94}O_4(OH)_2$ electrodes are shown in Figure 8b. The specific capacitances of $CaFe_{0.06}Ti_{1.94}O_4(OH)_2$ electrodes, calculated from discharge curves based on equation (1), were 964.3, 736.6, 582.6, and 519.0 $F \cdot g^{-1}$ at charge-discharge current densities of 10, 20, 50, and 100 $mA \cdot cm^{-2}$, respectively. The decreased specific capacitances could have contributed to the insufficient Faradic redox reactions at higher current densities.[33] The cycling behavior of $CaFe_{0.06}Ti_{1.94}O_4(OH)_2$ is shown in Figure 8c and the capacity observed to clearly increase in the first 100 cycles, which might have been because of electrode materials utilization activation. The specific capacities keep almost unchanged and remained 99.7% even after 5000 cycles, indicating a good candidate for supercapacitor application. To further understand the performance of $CaFe_{0.06}Ti_{1.94}O_4(OH)_2$ for electrochemical energy storage, the columbic efficiency of the sample is analysized (Fig. 8(d)). During the cyclic process, the columbic efficiency is 92%, indicating a good

capacity retention. Further demonstrating the practical application of our samples, the best optimum $CaFe_{0.06}Ti_{1.94}O_4(OH)_2$ electrode materials were assembled in CR2025-type coin cells. After charging for a short time, the sample device can easily power for a light-emitting diodes as shown in inset of Fig. 8(d), which indicates its future in practical application for supercapicators.

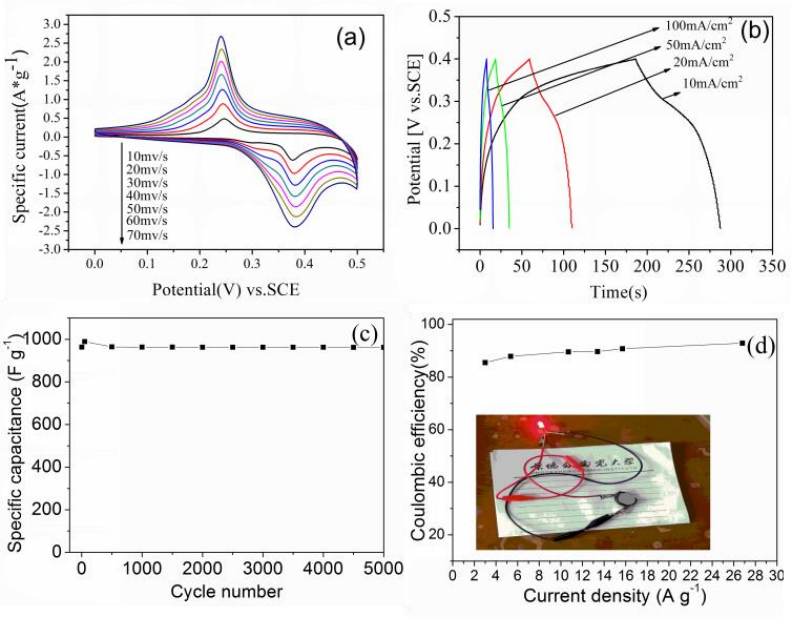

Figure 8. (a) the representative CV curves of the synthesized $CaFe_{0.06}Ti_{1.94}O_4(OH)_2$ electrodes within the potential range of 0 to 0.5 V (vs. SCE) at various scan rates from 10 to 70 mV s^{-1}; (b) The galvanostatic charge-discharge curves of the synthesized $CaFe_{0.06}Ti_{1.94}O_4(OH)_2$ electrodes in the voltage range of 0-0.5 V at charge-discharge current densities of 10 mA cm^{-2}, 20 mA cm^{-2}, 40 mA cm^{-2}, 50 mA cm^{-2} and 100 mA cm^{-2}; (c) the cyclic stability of the synthesized $CaFe_{0.06}Ti_{1.94}O_4(OH)_2$ electrodes at a current density of 10 mA cm^{-2}; (d) the columbic efficiency of the $CaFe_{0.06}Ti_{1.94}O_4(OH)_2$ sample. Inset of Fig. 8 (d) is the sample device easily powering for a light-emitting diodes after charging for a short time.

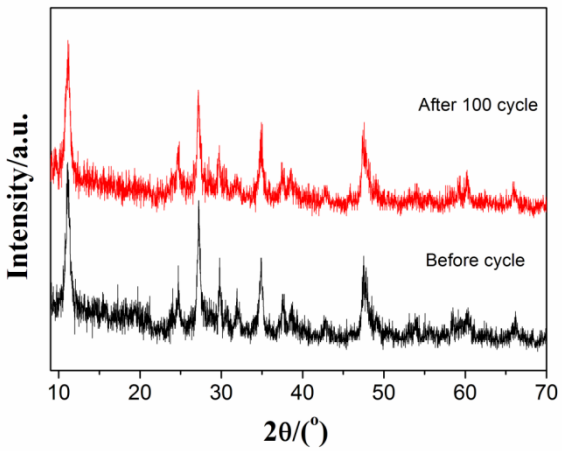

Figure 9. XRD patterns of the $CaTi_{1.94}Fe_{0.06}O_4(OH)_2$ sample after 100 charge/discharge cycles.

XRD patterns of $CaFe_{0.06}Ti_{1.94}O_4(OH)_2$ samples after 100 charge/discharge cycles showed that the patterns were similar to the original samples, indicating that the samples could recycle even after many charge/discharge cycles (Fig. 9). Only the peaks of the sample became broadened, indicating active materials pulverization during long-term cycles.

The present results demonstrated that $CaFe_{0.06}Ti_{1.94}O_4(OH)_2$ had the highest conductivity and possessed optimal electrochemical properties, which was attributed to morphological effects enhancing electrochemical activities [34] and smaller particles size that more easily accommodated structural changes during the cycling process.[35] In addition, the existence of Fe ions resulted in some local defects in the crystal structure, and thus increased electrical conductivity and ionic diffusion. Therefore, the cyclic performances of the $CaTi_2O_4(OH)_2$ system were apparently improved after introducing small amounts of Fe-doped ions. Complete clarification of Fe doping effects in the $CaTi_2O_4(OH)_2$ system requires further investigation.

Comparison of the electrochemical properties of similar electrode materials for supercapacitors reported in the literature and investigated here showed that, compared with many previous reports, $CaFe_{0.06}Ti_{1.94}O_4(OH)_2$ nanosheets had high capacity and superior rate capability (Table 2).

Table 2. Comparison of similar electrode materials and investigated material for supercapacitors

Electrode materials	Specific capacity	Rate performance	Ref.
Polypyrrole/MnO_2 on carbon cloth	325 F g^{-1} at 0.2 A g^{-1}	70% at a high current density of 5.0 A g^{-1}	[12]
Co_3O_4/reduced graphene oxide nanosheet composites	400 F g^{-1} at 0.5-2.0 A g^{-1}	-	[16]
Mesoporous weirds-like morphological MnO_2 thin films on carbon cloth	595 F g^{-1} at a scan rate of 5 mV s^{-1}	87% over 2,000 CV cycles	[17]
Graphene nanosheet(GNS)/kassite ($CaTi_2O_4(OH)_2$) composites	129.8 F g^{-1} at 1 A g^{-1}	-	[22]
N-doped graphene/Fe_2O_3 nanocomposite	698 F g^{-1} at 1 A g^{-1}	55% retention after 3000 cycles at 4 A g^{-1}	[32]
$CaFe_{0.06}Ti_{1.94}O_4(OH)_2$ nanosheet	964.3 F g^{-1} at 10 mA cm^{-2}	99.7 % retention after 5000 cycles at 10 mA cm^{-2}	This work

4. CONCLUSIONS

In summary, $CaFe_xTi_{2-x}O_4(OH)_2$ materials were successfully prepared by a simple solvothermal method. The results showed that sample electrochemical properties were enhanced after Fe ion doping into $CaTi_2O_4(OH)_2$. Electrochemical cells prepared with $CaFe_{0.06}Ti_{1.94}O_4(OH)_2$ cathode materials exhibited higher discharge capacity and better cyclic stability than undoped versions and other Fe-doped systems. The optimal composition of $CaFe_{0.06}Ti_{1.94}O_4(OH)_2$ presented 964.3 F·g^{-1} at a current

density of 10 $mA \cdot cm^{-2}$, 99.7% retention rate after 5000 cycles, and low charge-transfer resistance (2.41 $\Omega \cdot cm^2$). A suitable amount of Fe doping in $CaTi_2O_4(OH)_2$ system was successful for enhancing electrochemical properties by improving structural stability and electrical conductivity. The results of this study will contribute to furthering the applications of these materials in supercapacitors and also meaningful to future research.

ACKNOWLEDGMENTS
This work was supported by the major Natural Science Fund of Jiangxi Province (20152ACB21022) and National Natural Science Fund (51562013).

References

1. L. Zhang, X. Hu, Z. Wang and D. Dorrell, *Renew. Sustain. Energy Rev.*, 2 (2017) 1868.
2. T. Qin, S. Peng, J. Hao ,G. Cao, *Adv. Energy Mater.*, 20 (2017)1700409.
3. J. Y. Hwang, M. Li, M. El-Kady, R. Kaner, *Adv. Funct. Mater.*, 15 (2017)1605745.
4. Y. Jiang, J. Fletcher, P. Burr, C. Halla, B. Zheng, D. Wang, Z. Ouyanga and A. Lennon, *J. Power Sources*, 384 (2018) 396.
5. S. K. Kandasamy and K. Kandasamy, *J. Inorg. Organomet. P.*, 3(2018) 559.
6. B. Wang, J. Liu, F. Mirri, M. Pasquali, N. Motta and J. W. Holmes, *Nanotechnology*, **27** (2016)1.
7. A. J. Paleo, P. Staiti, A. Brigandì, F. N. Ferreira, A. M. Rocha and F. Lufrano, *Energy Storage Mater.*, 12 (2018) 204.
8. M. Huang, F. li, F. Dong and L. Zhang, *J. Mater. Chem.* A, 3 (2015) 21383.
9. H. Jia,Y. Cai, J. Lin and W. Fei, *Adv. Sci.*, 5(2018)1700887.
10. L. Wang,Y. Ouyang, X. Jiao and Q. Hao, *Chem. Eng. J.*, 334(2018) 1-9.
11. K. Ghosh and Y. Chee, *Electrochim. Acta*, 276, (2018) 47.
12. X. Fan, X. Wang, G. Li, A. Yu and Z. Chen, *J. Power Sources*, 326 (2016) 357-364.
13. G. Huang, Y. Zhang, L. Wang, P. Sheng and H. Peng, *Carbon*, 125(2017)595.
14. B. Patil, S. Ahn, S. Yu, H. Song, Y. Jeong, J. Kim and H. Ahn, *Carbon*, 134(2018)366.
15. L. Wang, Y. Ouyang, X. Jiao and Q. Hao, *Chem. Eng. J.*, 334(2017)1.
16. Z. Song, Y. Zhang, W. Liu and J. Qiu, *Electrochim. Acta*, 112 (2013)120.
17. P. A. Shinde, V. C. Lokhande, T. Ji and C. D. Lokhande, *J. Colloid. Interf. Sci.*, 498(2017) 202.
18. S. Chen,Y. Li, B. Wu, Z. Wu, F. Li, J. Wu, P. Liu and H. Li, *Electrochim. Acta*, 275 (2018) 40.
19. Z. Li, D. Zhao, C. Xu, J. Ning, Y. Zhong, Z. Zhang, Y. Wang and Y. Hu, *Electrochim. Acta*, 278(2018) 33.
20. N. Pu, C. Chen, H. Qiu, Y. Liu, C. Song, M. Lin and M. Ger, *Int. J. Electrochem. Sci.*, 13 (2018) 6812-6823.
21. Y. Zhu, Z. Wu, M. Jing, X. Yang, W. Song and X. Ji, *J. Power. Sources*, 273(2015) 584.
22. W. Meng, G. Zhao, B. Song, J. Xie, W. Lu and G. Han, *Appl. Phys.* A,123 (2017) 753.
23. W. Dong, B. Song, G. Zhao and G. Han, *Ceram. Int.*, 6(2013) 6795.
24. W. Dong, B. Song, G. Zhao and G. Han, *Int. J. Electrochem. Sc.*, 8(2013) 4551.
25. S. M. Malyovanyi, A, A. Andriiko and A, P. Monko, *J. Solid State Electrochem.*, 8(2003) 7.
26. M. Ren, Z. Zhou, Y. Li, X. P. Gao and J. Yan, *J. Power Sources*, 162 (2006) 1357.
27. S. Ma and H. Noguchi, *J Power Sources*, 161 (2006) 1297.
28. B. D. Cullity, Elements of X-Ray Diffraction, 2nd ed., Addison-Wesley, London, 1978
29. G. M. Sheldrick, *Acta Crys.* A, 46 (1990) 467
30. G. Huang, H. Liu, S. Wang and M. Xu, *J. Mater. Chem.* A, 2015
31. M. Li, C. Liu, H. Cao and Z. Fan, *J. Mater. Chem.* A, 2(2014)14844.
32. F. Wang, G. Li, J. Zheng, J. Ma, C. Yang and Q. Wang, *J. Colloid. Interf. Sci.*, 516(2018) 48.

33. A. D. Robertson, H. Takamoto and J. T. S. Irvine, *J. Electrochem. Soc*. 146 (1999) 3958.
34. G. Zhou, D. Wang, F. Li and H. Cheng, *Carbon*, 3(2011) 180.
35. F. C. Bazito, R. M. Torresi and J. Braz, *Chem. Soc*. 17 (2006) 627.